

Supporting Information:

Time-resolved single-particle x-ray scattering reveals electron-density gradients as coherent plasmonic-nanoparticle-oscillation source

Dominik Hoeing,^{†,‡} Robert Salzwedel,[¶] Lena Worbs,^{§,||} Yulong Zhuang,[⊥]
Amit K. Samanta,[§] Jannik Lübke,^{§,†,||} Armando D. Estillore,[§] Karol
Dlugolecki,[§] Christopher Passow,[#] Benjamin Erk,[#] Nagitha Ekanayake,[#]
Daniel Ramm,[#] Jonathan Correa,[#] Christina C. Papadopoulou,[#] Atia Tul
Noor,[#] Florian Schulz,^{||} Malte Selig,[¶] Andreas Knorr,^{*,¶} Kartik Ayyer,^{*,†,⊥}
Jochen Küpper,^{*,§,†,||,‡} and Holger Lange^{*,†,‡}

[†]*Center for Ultrafast Imaging, Universität Hamburg, 22761 Hamburg, Germany*

[‡]*Department of Chemistry, Universität Hamburg, 20146 Hamburg, Germany*

[¶]*Institut für Theoretische Physik, Technische Universität Berlin, 10623 Berlin, Germany*

[§]*Center for Free-Electron Laser Science CFEL, Deutsches Elektronen-Synchrotron DESY, 22607
Hamburg, Germany*

^{||}*Department of Physics, Universität Hamburg, 22761 Hamburg, Germany*

[⊥]*Max Planck Institut for the Structure and Dynamics of Matter, 22761 Hamburg Germany*

[#]*Deutsches Elektronen-Synchrotron DESY, 22607 Hamburg, Germany*

E-mail: andreas.knorr@tu-berlin.de; kartik.ayyer@mpsd.mpg.de;

jochen.kuepper@cfel.de; holger.lange@uni-hamburg.de

1. Methods

1.1 Particle Synthesis

Tetrachloroauric(III) acid (HAuCl_4 , $\geq 99.9\%$ trace metals basis), hexadecyltrimethylammonium bromide (CTAB, $\geq 98\%$) and chloride (CTAC, $\geq 98\%$), l-ascorbic acid (AA, reagent grade) and sodium borohydride (NaBH_4 , $\geq 98\%$) were purchased from Sigma-Aldrich (USA). All reagents were used as received. Ultrapure water was used for all procedures.

Spherical gold nanoparticles (AuNPs) were synthesized according to a modified protocol by Zheng et al.^{1,2} The protocol starts by producing Au clusters, followed by two growth steps. Au clusters were synthesized by adding 600 μL of an aqueous solution of NaBH_4 (10 mM) to a mixture of 0.1 ml HAuCl_4 (0.25 mM) and 10 mL CTAB (100 mM) via one-shot injection. The solution was rapidly stirred at 700 rpm during injection and for an additional 3 minutes. The solution was then kept undisturbed for 3 hours yielding Au clusters stabilized by CTAB.

The clusters were grown to 10.6 nm AuNPs by a one-shot-injection of the seed solution (50 μL) into a mixture of HAuCl_4 (2 ml, 0.5 mM), CTAC (2 ml, 200 mM) and ascorbic acid (AA, 1.5 ml, 100 mM). The solution was stirred for 15 minutes at 300 rpm and then washed twice by centrifugation (20 000 G, 1 h and 30 min, respectively) and replacement of the supernatant with a fresh CTAC solution (10 ml, 20 mM). The particle sizes were then increased again by a second growth step: A solution of the 10.6 nm AuNPs (3.6 mL) was mixed with a CTAC solution (120 ml, 100 mM). AA (780 μL , 100 mM) was added and after 60 s, HAuCl_4 (120 ml, 0.5 mM) was added dropwise within 1 hour with a syringe pump at a constant rate of 120 ml/h. The solution was stirred throughout the addition of AA and HAuCl_4 and for an additional 10 minutes at 300 rpm. The solution was washed and the concentration increased by centrifugation and replacement of the supernatant with sequentially less volume of fresh CTAC solution (5000 G, 2x 40 min and 3x 20 min). After the second centrifugation and redispersion step, the solution was transferred from 40 ml to (several) 1.5 ml centrifugation tubes. The final pellet was redispersed in 6 ml CTAC (20 mM) yielding a AuNP concentration of 12.9 nM (7.76×10^{12} particles/ml).

1.2 Sample characterization

UV-Vis spectroscopy

Absorption spectra were recorded using a Varian Cary 50 spectrometer. The concentrated AuNP dispersion was diluted by a factor of 1:100 and its absorbance at 450 nm was used to determine the concentration according to Haiss et al.³ The measured spectrum is plotted in Fig. S1. The shape of the plasmon-related absorption around 525 nm confirms isolated spherical AuNPs.

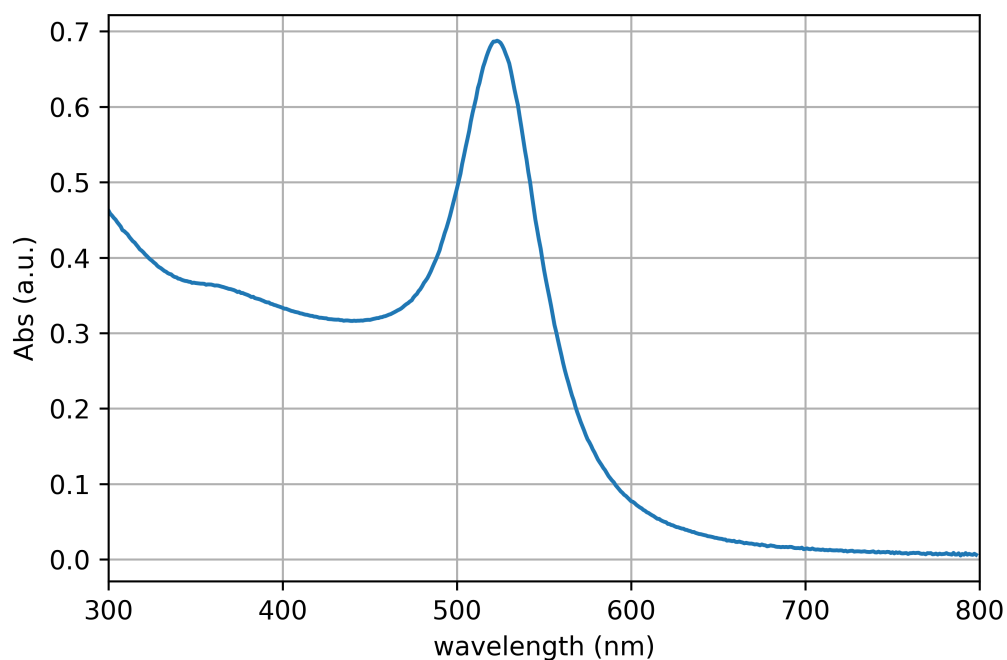


Figure S1: UV-Vis spectrum of the employed AuNP solution.

Transmission electron microscopy

Transmission electron microscopy (TEM) was used to determine the AuNP size distributions. Because of the TEM contrast depending on the material's atomic number, particle sizes without contributions of the ligand layer are obtained, which is advantageous for a comparison with the results from the X-ray scattering experiment. According to the TEM analysis, the AuNPs used in the experiments were 27.1 nm in diameter with a standard deviation of 0.8 nm. Representative TEM images and the size histogram are displayed in Fig. S2.

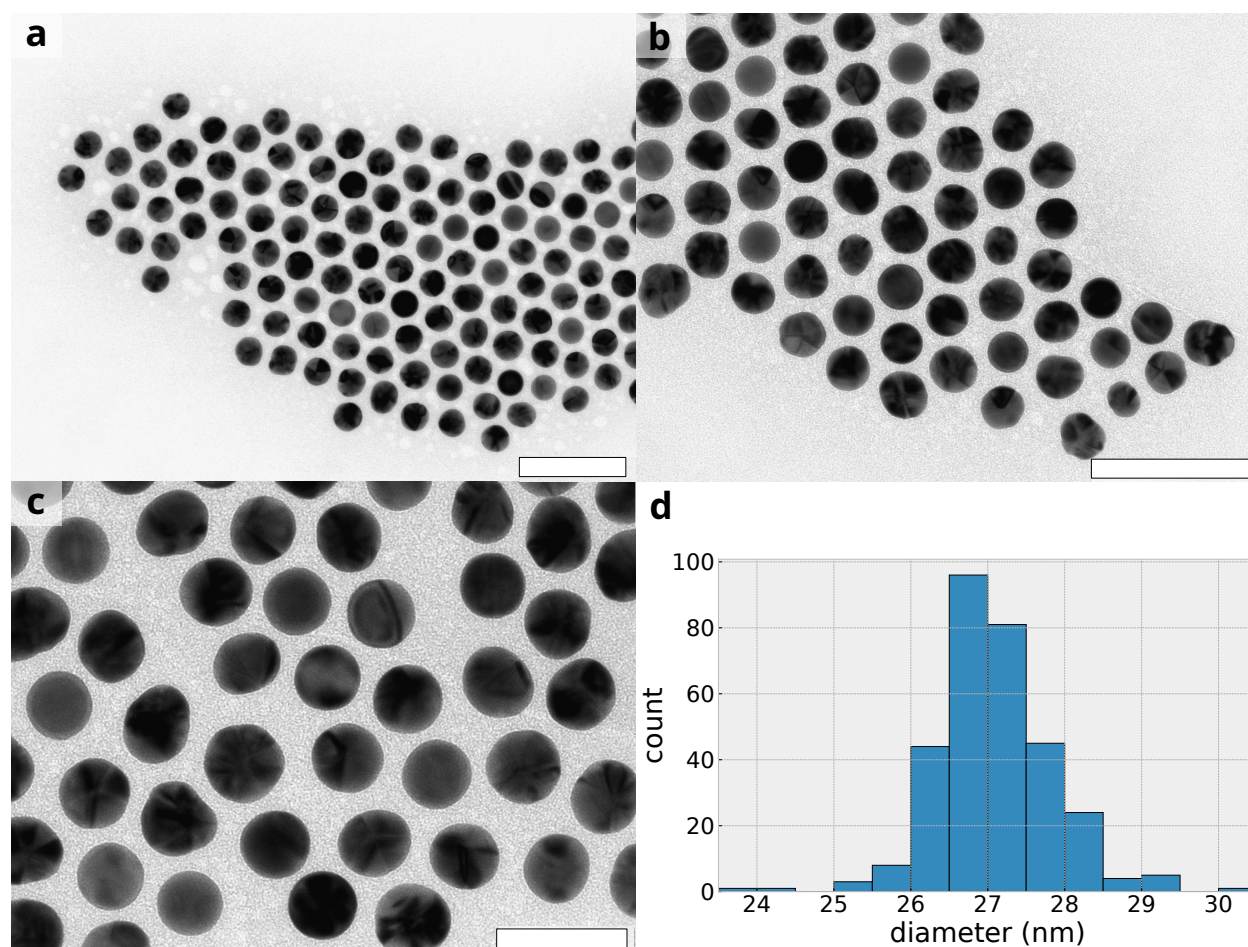


Figure S2: (a-c) Representative TEM images and (d), size histogram of the employed AuNPs. The scale bars measure 200 nm (a), 100 nm (b) and 50 nm (c). The average particle diameter is (27.1 ± 0.8) nm.

1.3 Transient Absorption Spectroscopy

Ultrashort laser pulses with a center wavelength of 800 nm were generated in a chirped pulse amplifier (Spectra Physics Spitfire) at a repetition rate of 1 kHz. The amplifier was seeded by a Ti:sapphire oscillator (Spectra Physics MaiTai) and pumped by a Nd:YBG laser (Spectra Physics Empower). The output of the regenerative amplifier is split into two arms, which are compressed individually. The pulse length was 35 fs as determined by autocorrelation. One arm was sent through a BBO crystal to produce pump pulses with a center wavelength of 400 nm. Every second pump pulse was blocked by a chopper running at 500 Hz for referencing every pumped spectrum with a ground-state spectrum. The pump power was set to 0.7 and 1.8 mJ/cm² using a variable neutral density filter. Additionally, to study the phase-dependence of the breathing oscillation, 0.5, 1.0 and 2.0 mJ/cm² were applied. Because of the use of transmissive optical elements, an induced chirp is present, which results in an increase in pulse duration. However, due to the limited number of optical elements we expect the pump pulses to be shorter than 150 fs. The second (probe) arm was aligned through a delay stage and onto a sapphire crystal for white-light generation in the transient absorption spectrometer (Ultrafast Systems Helios). The white-light transmitted through the sample was focused on a UV-Vis spectrometer with a 1024 pixel CMOS sensor. The TA data was corrected for optical chirp and scattering around the pump wavelength. To obtain the e-ph time constants. Time-zero was set to the time of maximum pump and probe overlap, which is also the point of maximum bleach contrast in the data set. The local minimum of the bleach signal at each delay time was determined using a gaussian function. Note that the TA minimum blueshifts within the first few picoseconds and therefore analyzing the bleach signal at a fixed probe wavelength can produce errors.⁴ The obtained minimum of the bleach intensity vs. delay time was then normalized and fitted with a bi-exponential decay function. The time constants of the decay are interpreted as coupling times:

$$\Delta A(t) = a \cdot \exp\left(-\frac{t}{\tau_{e-ph}}\right) + b \cdot \exp\left(-\frac{t}{\tau_{ph-ph}}\right),$$

where τ_{e-ph} is the electron-phonon coupling time τ_{ph-ph} the longer coupling to the environment (phonon-phonon) and a, b are the relative weights as additional fit parameters .

The periodic oscillation of the AuNP size due to an excited breathing oscillation leads to a periodic red-shift of the plasmon absorption because of the variation in electron density (constant number of electrons for varying AuNP volume). In TA, the breathing mode is observable at the long-wavelength shoulder of the plasmon absorption, where the oscillation of the TA signal is superimposed with the contrast due to electron cooling. Here, we analyzed the breathing mode by probing ΔA at 545 nm. To aid understanding the origin of the TA spectra in Fig. 2 in the main text, Fig. S3 displays absorption spectra at different delay times. 1 ps prior to the pump pulse arrival, the sample is in its ground state. 0.5 ps after pulsed excitation, the difference between ground state absorption and excited state absorption is maximal. The differential spectrum is discussed in Fig. 2 of the main text.

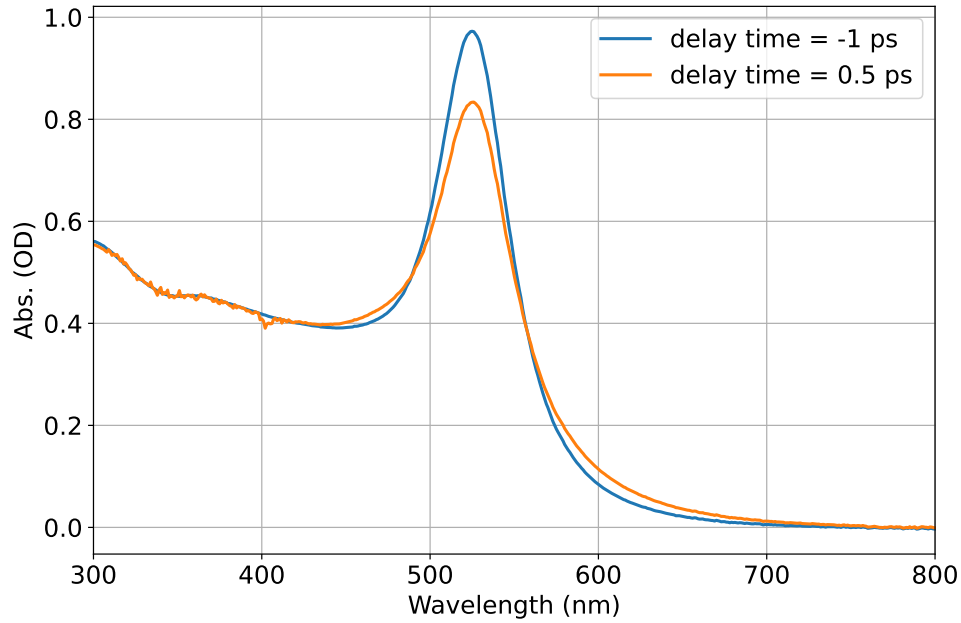


Figure S3: Absorption spectra before (-1 ps) and shortly after (0.5 ps) the pulsed excitation of the AuNPs with 400 nm excitation wavelength and 1.8 mJ/cm^2 laser pulses.

1.4 Transient small-angle x-ray scattering

The experiment was conducted using the CAMP end-station at beamline BL1 of the FLASH facility at DESY,⁵ extended by a user-provided injection system.^{6,7} The free-electron laser (FEL) provided bursts of X-ray pulses with a photon energy of 275.5 eV and an intra-train repetition rate of 250 kHz. Each pulse train consisted of 100 pulses and the average fluence per pulse at the focus position was approximately $6 \cdot 10^9$ photons/mm². From indirect measurement of the electron pulse duration before the undulators, we estimate an FEL pulse duration of 120 fs. The optical pump pulses were provided by a chirped pulse optical parametric amplifier (OPCPA)⁸ with an output wavelength of (402.0 ± 3.3) nm, a pulse duration of 80 fs and a repetition rate of 500 kHz. The pump pulses excited individual AuNPs and the scattering of time-delayed x-ray pulses was measured by large-area pnCCD photon detectors read-out at 10 Hz.^{9,10}

Prior to the measurements, the spatial overlap of the injected particles, the FEL and the pump laser was established by focusing the FEL, the pump laser, and a frequency doubled Nd:YAG laser for particle detection on the same position of a retractable YAG screen.¹¹ The temporal overlap of the FEL and pump pulses was ensured by measuring the transient reflectivity of a Si₃N₄ film that was moved into the focus position, with x-ray excitation leading to an increased optical reflectivity of the Si₃N₄ film¹² for the pump pulses. Our data suggests a < 500 fs temporal resolution of the experiment. After retracting the screens, the particle beam was adjusted by maximizing scattering of the particle-detection laser by injected sucrose particles and 80 nm AuNPs.

For sample injection, an AuNP aerosol was created using a commercial electrospray (TSI Advanced Electrospray 3482). Two differential pumping stages were used to remove excess nitrogen and CO₂ and the AuNP beam was generated using an optimized aerodynamic lens stack (ALS).^{6,7,13} The injector pressure was kept at 1.0 mbar. The injector was tested prior to x-ray imaging by optical scattering off sucrose particles using a frequency doubled Nd:YAG laser (Innova SpitLight) and a camera-based microscope system. The particle detection laser was turned off during the imaging experiments.

1.5 Data analysis of transient small-angle x-ray scattering patterns

Classification with *Dragonfly*

In an aerosol serial diffraction experiment, most XFEL pulses do not intercept a particle in the focus. Those that do, commonly termed ‘hits’, are detected by a straightforward total signal threshold on the diffracted data. But not all hits are useful since the aerosolization process produces signal from many objects other than spherical AuNPs. This includes multi-particle aggregates, ellipsoidal particles as well as patterns resulting from detector artifacts or cosmic rays. In order to extract the small signal from these patterns, one must find and reject these other hits. This classification was performed using the *Dragonfly*¹⁴ software which uses a modified version of the EMC algorithm¹⁵ in order to statistically align and average similar patterns into multiple class averages. The procedure was similar to that described in detail in¹⁶ for classifying patterns from faceted AuNPs while taking into account in-plane rotation and detector panel gaps and bad pixels.

Figure S4 shows some representative class averages. We removed frames that were classified as contamination and multiple hits (top left and right panels) as well as ellipsoidal particles (bottom right panel) and only kept the single hits frames of spherical particles (bottom left panel).

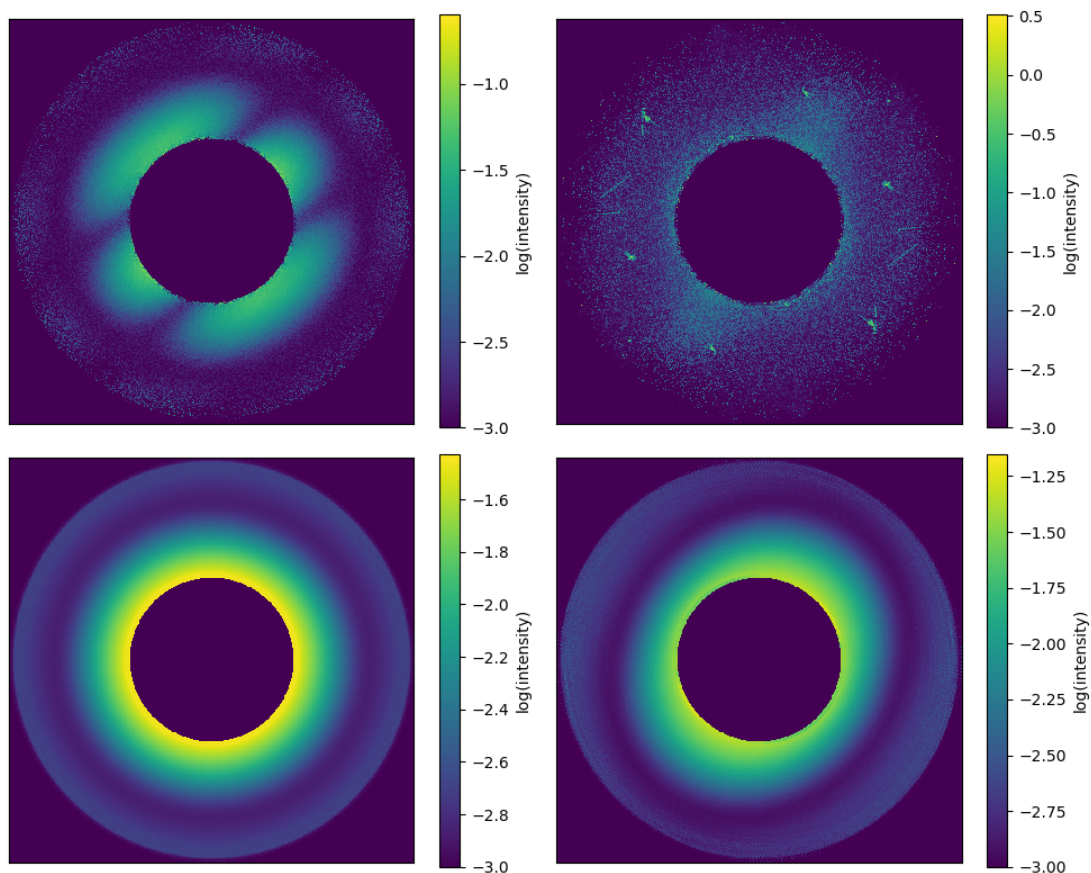


Figure S4: Four typical patterns from Dragonfly classifications. Top left: multiple hits; top right: contaminations; bottom left: single hits of spherical AuNPs; bottom right: single hits of ellipsoidal particles.

Diameter fitting

All 2D class averages of single particles were fit with a function representing the diffraction from an ellipsoidal object. This resulted in three parameters per average, the major and minor axes as well as the tilt of the major axis. Only patterns belonging to class averages with a low eccentricity were included in further analysis. Since the EMC algorithm assigns each pattern a probability distribution over the various models, one can determine each AuNP's diameter by taking the weighted mean of the model diameters, with the weights obtained from the probabilistic assignment made by *Dragonfly*.

Average diameter vs pump-probe delay

In order to avoid experimental drifts, data was collected by continuously oscillating the pump-probe delay between -3 ps and +22 ps at a rate of 0.1 ps/s. Thus, in general, each measurement was obtained from a random delay time in this range. In order to aggregate the mean diameter at a given central delay time, the diameters of all patterns with a delay ± 1 ps from the central time were averaged. This bin width of 2 ps was chosen to balance the needs of observing the details of the oscillatory behavior with obtaining sufficient statistics. The bin centers were sampled every 0.1 ps in order to generate the data shown in Fig. 3 and Fig. 4a in the main text.

2. Theory of electric and thermal sources to the oscillation

Our theoretical framework is based on a Heisenberg equation of motion framework that allows one to derive the AuNP size oscillation from the following Hamiltonian:

$$\begin{aligned}
 H = & \sum_{\mathbf{k}, \lambda} \epsilon_{\mathbf{k}}^{\lambda} \lambda_{\mathbf{k}}^{\dagger} \lambda_{\mathbf{k}} + \sum_{\mathbf{q}} \hbar \omega_{\mathbf{q}} b_{\mathbf{q}}^{\dagger} b_{\mathbf{q}} - \sum_{\mathbf{k}, \mathbf{K}, \lambda} \mathbf{d}^{\lambda \bar{\lambda}} \cdot \mathbf{E}_{-\mathbf{K}} \lambda_{\mathbf{k}}^{\dagger} \bar{\lambda}_{\mathbf{k}+\mathbf{K}} \\
 & + \sum_{\mathbf{q}, \mathbf{k}, \lambda} g_{\mathbf{q}}^{\lambda} \lambda_{\mathbf{k}+\mathbf{q}}^{\dagger} \lambda_{\mathbf{k}} \left(b_{\mathbf{q}} + b_{-\mathbf{q}}^{\dagger} \right) + \frac{1}{2} \sum_{\substack{\mathbf{k}, \mathbf{k}', \mathbf{q} \\ \lambda \lambda'}} V_{\mathbf{q}} \lambda_{\mathbf{k}+\mathbf{q}}^{\dagger} \lambda_{\mathbf{k}'-\mathbf{q}}^{\dagger} \lambda_{\mathbf{k}'} \lambda_{\mathbf{k}} \\
 & + \sum_{\mathbf{q}_1 \mathbf{q}_2 \mathbf{q}_3} h_{\mathbf{q}_1 \mathbf{q}_2 \mathbf{q}_3} \left(b_{\mathbf{q}_1} + b_{-\mathbf{q}_1}^{\dagger} \right) \left(b_{\mathbf{q}_2} + b_{-\mathbf{q}_2}^{\dagger} \right) \left(b_{\mathbf{q}_3} + b_{-\mathbf{q}_3}^{\dagger} \right).
 \end{aligned} \tag{1}$$

The first term accounts for the electron dispersion $\epsilon_{\mathbf{k}}^{\lambda}$ in the AuNP with electronic annihilation (creation) operators $\lambda_{\mathbf{k}}^{(\dagger)}$ with momentum \mathbf{k} in the band λ , that allows one to treat the combined effect of intraband and interband transitions coupled to acoustic phonons.^{17,18} The second term incorporates the dispersion $\hbar \omega_{\mathbf{q}}$ of dominant longitudinal acoustic (LA) phonon modes with phonon annihilation (creation) operators $b_{\mathbf{q}}^{(\dagger)}$ with momentum \mathbf{q} . In the Debye approximation,^{19,20} the appearing phonon dispersion is assumed to be linear $\omega_{\mathbf{q}} = c_{LA} |\mathbf{q}|$ with the velocity of sound c_{LA} .²¹ The third term describes the interband part of the semiclassical light-matter coupling^{22,23} with the transition dipole matrix element $\mathbf{d}^{\lambda \bar{\lambda}} = 1/\Omega \int_{UC} u_{\lambda}^*(\mathbf{r}) e \mathbf{r} u_{\bar{\lambda}}(\mathbf{r}) d^3 r$ and the Fourier component $\mathbf{E}_{\mathbf{K}}(t)$ of the exciting electric field $\mathbf{E}(\mathbf{r}, t) = \sum_{\mathbf{K}} \exp\{i \mathbf{K} \cdot \mathbf{r}\} \mathbf{E}_{\mathbf{K}}(t)$. As the experiment is carried out in a spectral region where interband transitions dominate the material response (cf.²⁴), only the interband light-matter coupling will be considered in the following. The first term in the second line considers the electron-phonon interaction with the electron-phonon coupling strength $g_{\mathbf{q}}^{\lambda} = -i \sqrt{\hbar N / 2 M \omega_{\mathbf{q}}} [\mathbf{A}_{\mathbf{q}} \cdot \mathbf{q}] \Phi_{\mathbf{q}}^{\lambda}$,²⁰ where M is the ion mass in the unit cell, N is the ion number in the crystal, and $\mathbf{A}_{\mathbf{q}}$ are the phonon polarization vectors given by $\mathbf{A}_{\mathbf{q}} = \frac{\mathbf{q}}{|\mathbf{q}|}$ for the case of LA phonons.²⁵ $\Phi_{\mathbf{q}}^{\lambda}$ is the Fourier transformed ion electron-ion potential for the respective band λ .²⁶ The second term in that line accounts for the carrier-carrier Coulomb interaction $V_{\mathbf{q}} = e^2 / \epsilon(\mathbf{q}) V q^2$ with momentum exchange \mathbf{q} between two carrier with momenta \mathbf{k} and \mathbf{k}' and the crystal volume

V. The third line describes the phonon-phonon interaction occurring from anharmonic corrections in the ion-ion interaction. The appearing matrix element conserves the total momentum of the involved phonons, i.e. $h_{\mathbf{q}_1\mathbf{q}_2\mathbf{q}_3} = \tilde{h}_{\mathbf{q}_1\mathbf{q}_2\mathbf{q}_3}\delta_{\mathbf{q}_1+\mathbf{q}_2+\mathbf{q}_3,0}$.

We define the microscopic phonon mode amplitude $s_{\mathbf{q}}$ that determines the macroscopic lattice displacement (Eq. (1) in the main document) and the Wigner functions for the band occupation $f_{\mathbf{k}}^{\lambda}(\mathbf{r})$ and the interband coherence $p_{\mathbf{k}}(\mathbf{r})$ for an effective two-band model with a derived susceptibility that can be obtained from the experiment:

$$s_{\mathbf{q}}(t) = \frac{1}{2} \left(\langle b_{\mathbf{q}} \rangle (t) + \langle b_{-\mathbf{q}}^{\dagger} \rangle (t) \right), \quad (2)$$

$$f_{\mathbf{k}}^{\lambda}(\mathbf{r}, t) = \sum_{\mathbf{q}} e^{i\mathbf{q}\cdot\mathbf{r}} \langle \lambda_{\mathbf{k}-\mathbf{q}}^{\dagger} \lambda_{\mathbf{k}} \rangle (t), \quad (3)$$

$$p_{\mathbf{k}}(\mathbf{r}, t) = \sum_{\mathbf{q}} e^{i\mathbf{q}\cdot\mathbf{r}} \langle v_{\mathbf{k}-\mathbf{q}}^{\dagger} c_{\mathbf{k}} \rangle (t). \quad (4)$$

In gold, the interband transitions occur between the initially occupied and the initially unoccupied band²⁷ that are below (above) the Fermi level respectively. Accordingly, they are labeled as v for valence and c for conduction band. The equation of motion for the phonon mode amplitude reads:

$$\left(\partial_t^2 + 2\gamma_{\text{ph}}^{\mathbf{q}} \partial_t + \omega_{\mathbf{q}}^2 \right) s_{\mathbf{q}}(t) = -\frac{\omega_{\mathbf{q}}}{\hbar} \sum_{\mathbf{k}} \left(g_{-\mathbf{q}}^c - g_{-\mathbf{q}}^v \right) \tilde{f}_{\mathbf{k}}^c(\mathbf{q}, t) \quad (5)$$

$$- \frac{3\omega_{\mathbf{q}}}{\hbar} \sum_{\mathbf{k}} \tilde{h}_{-\mathbf{q},\mathbf{k},\mathbf{q}-\mathbf{k}} \delta \tilde{n}_{\mathbf{k}}(\mathbf{q}, t). \quad (6)$$

This equation describes the dynamics of a classical damped oscillator equation with mode index \mathbf{q} . The left-hand side describes the oscillation of the coherent phonon amplitude $s_{\mathbf{q}}$ with a damping rate $\gamma_{\text{ph}}^{\mathbf{q}}$ ²⁸ resulting from phonon-phonon interactions, treated here as a constant. On the right-hand side, two sources to the oscillation of the coherent phonon mode amplitude are identified. The first term is determined by the dynamics of the Fourier transform of the occupation Wigner function $\tilde{f}_{\mathbf{k}}^{\lambda}(\mathbf{q}) = \langle \lambda_{\mathbf{k}-\mathbf{q}}^{\dagger} \lambda_{\mathbf{k}} \rangle$ showing that a spatial inhomogeneous electron distribution drives $s_{\mathbf{q}}$.²⁹

The prefactor scales with the difference $(g_{-\mathbf{q}}^c - g_{-\mathbf{q}}^v)$ of the electron-phonon coupling element of conduction and valence band. The second source of the coherent phonon amplitude results from thermal effects of the change of the phonon occupation caused by electron heating from its equilibrium value: $\delta\tilde{n}_{\mathbf{k}}(\mathbf{q}, t) = \tilde{n}_{\mathbf{k}}(\mathbf{q}, t) - \tilde{n}_{\mathbf{k}}(\mathbf{q}, t \rightarrow -\infty)$ where we define $\tilde{n}_{\mathbf{k}}(\mathbf{q}, t) = \langle b_{\mathbf{k}-\mathbf{q}}^\dagger b_{\mathbf{k}} \rangle(t)$. The constant contributions from the right side (equilibrium electron density and equilibrium phonon density) were absorbed in the equilibrium position of the oscillator, so that only deviations from equilibrium act as sources for the oscillation.

As the Wigner occupations $f_{\mathbf{k}}^\lambda(\mathbf{r})$ act as sources of the coherent phonon amplitude Eq. (5), we also derive an equation of motion for a two band model within the gradient expansion²⁹ and obtain

$$\partial_t f_{\mathbf{k}}^v(\mathbf{r}) = -\mathbf{v}_{\mathbf{k}}^v \cdot \nabla_{\mathbf{r}} f_{\mathbf{k}}^v(\mathbf{r}) - 2 \operatorname{Im} \left\{ \frac{\mathbf{d}^{vc} \cdot \mathbf{E}(\mathbf{r}, t)}{\hbar} p_{\mathbf{k}}(\mathbf{r}) \right\} - \frac{1}{\tau} (f_{\mathbf{k}}^v(\mathbf{r}) - f_{\mathbf{k}}^{v,0}(\mathbf{r})) \quad (7)$$

$$\partial_t f_{\mathbf{k}}^c(\mathbf{r}) = -\mathbf{v}_{\mathbf{k}}^c \cdot \nabla_{\mathbf{r}} f_{\mathbf{k}}^c(\mathbf{r}) + 2 \operatorname{Im} \left\{ \frac{\mathbf{d}^{vc} \cdot \mathbf{E}(\mathbf{r}, t)}{\hbar} p_{\mathbf{k}}(\mathbf{r}) \right\} - \frac{1}{\tau} (f_{\mathbf{k}}^c(\mathbf{r}) - f_{\mathbf{k}}^{c,0}(\mathbf{r})) \quad (8)$$

$$\begin{aligned} \partial_t p_{\mathbf{k}}(\mathbf{r}) = & \left[-\frac{i}{\hbar} (\epsilon_{\mathbf{k}}^c - \epsilon_{\mathbf{k}}^v) - \gamma - \frac{(\mathbf{v}_{\mathbf{k}}^c + \mathbf{v}_{\mathbf{k}}^v)}{2} \cdot \nabla_{\mathbf{r}} \right] p_{\mathbf{k}}(\mathbf{r}) \\ & + i \frac{\mathbf{d}^{cv} \cdot \mathbf{E}(\mathbf{r}, t)}{\hbar} [f_{\mathbf{k}}^v(\mathbf{r}) - f_{\mathbf{k}}^c(\mathbf{r})] \end{aligned} \quad (9)$$

In Eqs. (7,8), we identify the group velocity $\mathbf{v}_{\mathbf{k}}^\lambda = \nabla_{\mathbf{k}} \epsilon_{\mathbf{k}}^\lambda / \hbar$ for the band λ that considers the drift of the electronic Wigner occupation. The term on the right-hand side in Eqs. (7,8) accounts for the optical source via the full electric field $\mathbf{E}(\mathbf{r}, t)$ that includes the external field as well as polarization contributions. In Eq. (9), the interband polarization oscillates with the band gap $(\epsilon_{\mathbf{k}}^c - \epsilon_{\mathbf{k}}^v)$ and is also driven by the external optical driving field $\mathbf{E}(\mathbf{r}, t)$. γ is the electron-electron scattering induced damping term of the order of few femtoseconds³⁰ for the interband transition and was added phenomenologically. The radiative lifetime of the band occupations, denoted by τ , was added phenomenologically and is estimated to be a few picoseconds.

In the following we expand the individual Wigner functions in orders of the electric field $f_{\mathbf{k}}^\lambda(\mathbf{r}, t) = f_{\mathbf{k}}^{0,\lambda}(\mathbf{r}) + f_{\mathbf{k}}^{1,\lambda}(\mathbf{r}, t) + f_{\mathbf{k}}^{2,\lambda}(\mathbf{r}, t) + \mathcal{O}(\mathbf{E}^3)$ and $p_{\mathbf{k}}(\mathbf{r}, t) = p_{\mathbf{k}}^1(\mathbf{r}, t) + p_{\mathbf{k}}^2(\mathbf{r}, t) + \mathcal{O}(\mathbf{E}^3)$, enter a rotating

frame $\mathbf{E}(\mathbf{r}, t) = \tilde{\mathbf{E}}^+ e^{i\omega_{\text{opt}} t} + \tilde{\mathbf{E}}^- e^{-i\omega_{\text{opt}} t}$ and $p_{\mathbf{k}}(\mathbf{r}, t) = \tilde{p}_{\mathbf{k}}(\mathbf{r}, t) e^{-i\omega_{\text{opt}} t}$ and apply a rotating wave approximation. Assuming a fast dephasing γ , we solve the equation for the interband coherence adiabatically and also neglect the transport terms in Eqs. (9,8,7) as they are also small compared the individual time dynamics. Since the spatial gradients needed to evaluate the displacement Eq. (16) is mainly determined by the dielectric, off-resonant contribution, we replace the full self-consistent field by the field $\tilde{\mathbf{E}}_B$ formed by the dielectric background. In addition, a radiation self energy correction will be absorbed in the frequency $\omega_{\mathbf{k}} \equiv (\epsilon_{\mathbf{k}}^c - \epsilon_{\mathbf{k}}^v) \hbar \rightarrow \tilde{\omega}_{\mathbf{k}}$ and the dephasing $\gamma \rightarrow \tilde{\gamma}$. Thus, the governing equations for the band occupations read

$$\partial_t f_{\mathbf{k}}^{c,2}(\mathbf{r}, t) = \left| \frac{\mathbf{d}^{vc} \cdot \tilde{\mathbf{E}}_B(\mathbf{r}, t)}{\hbar} \right|^2 \frac{2\tilde{\gamma}}{\tilde{\gamma}^2 + (\tilde{\omega}_{\mathbf{k}} - \omega_{\text{opt}})^2} [f_{\mathbf{k}}^{v,0}(\mathbf{r}) - f_{\mathbf{k}}^{c,0}(\mathbf{r})] - \frac{1}{\tau} f_{\mathbf{k}}^{c,2}(\mathbf{r}), \quad (10)$$

$$\partial_t f_{\mathbf{k}}^{v,2}(\mathbf{r}, t) = - \left| \frac{\mathbf{d}^{vc} \cdot \tilde{\mathbf{E}}_B(\mathbf{r}, t)}{\hbar} \right|^2 \frac{2\tilde{\gamma}}{\tilde{\gamma}^2 + (\tilde{\omega}_{\mathbf{k}} - \omega_{\text{opt}})^2} [f_{\mathbf{k}}^{v,0}(\mathbf{r}) - f_{\mathbf{k}}^{c,0}(\mathbf{r})] - \frac{1}{\tau} f_{\mathbf{k}}^{v,2}(\mathbf{r}). \quad (11)$$

In the following, we apply a coarse-graining procedure using the macroscopic definition of the lattice displacement (Eq. 1 in the main manuscript) and a momentum expansion for the Wigner occupations given by:

$$\rho^\lambda(\mathbf{r}, t) \equiv \frac{e}{\Omega} \sum_{\mathbf{k}} f_{\mathbf{k}}^\lambda(\mathbf{r}, t), \quad (12)$$

with the unit cell volume Ω . This allows to identify the contribution of the interband transitions via the macroscopic susceptibility:

$$\chi^{\text{inter}}(\omega) = - \frac{|d|^2}{\hbar \epsilon_0 \Omega} \sum_{\mathbf{k}} \frac{f_{\mathbf{k}}^{v,0}(\mathbf{r}) - f_{\mathbf{k}}^{c,0}(\mathbf{r})}{\omega - \tilde{\omega}_{\mathbf{k}} + i\tilde{\gamma}}, \quad (13)$$

resulting in macroscopic equations for the carrier densities:

$$\partial_t \rho_2^v(\mathbf{r}, t) = - \frac{2e\epsilon_0}{\hbar} \left| \tilde{\mathbf{E}}_B(\mathbf{r}, t) \right|^2 \text{Im} \{ \chi^{\text{inter}}(\omega_{\text{opt}}) \} - \frac{1}{\tau} \rho_2^v(\mathbf{r}, t), \quad (14)$$

$$\partial_t \rho_2^c(\mathbf{r}, t) = \frac{2e\epsilon_0}{\hbar} \left| \tilde{\mathbf{E}}_B(\mathbf{r}, t) \right|^2 \text{Im} \{ \chi^{\text{inter}}(\omega_{\text{opt}}) \} - \frac{1}{\tau} \rho_2^c(\mathbf{r}, t). \quad (15)$$

These equations describe the occupation dynamics for the individual bands with a source term that creates or annihilates density in the respective band due to the presence of an external field $\tilde{\mathbf{E}}_0(\mathbf{r}, t)$.

Using the definition of the lattice displacement $\mathbf{u}(\mathbf{r}, t)$, the equation for the lattice displacement can be found:

$$[\partial_t^2 + 2\gamma_{\text{ph}}\partial_t - c_{LA}^2\nabla_{\mathbf{r}}^2] \mathbf{u}(\mathbf{r}, t) = \zeta \nabla \rho_2^c(\mathbf{r}, t) + \xi [T(t) - T_0]. \quad (16)$$

The temperature dependence is obtained within a Debye approximation for the incoherent phonon distribution. We find two driving terms with prefactors ζ and ξ that characterize the macroscopic model. The first represents the newly found displacement source resulting from an optically induced gradient in the spatial electron distribution $\rho_2^c(\mathbf{r}, t)$. This spatial gradient in the electron density is identified as the dominating origin of the optically induced oscillation of the displacement since it can explain the onset of the oscillation, measured to be faster than the thermal contributions (second term) in Eq. (16). The prefactor ζ scales with the difference of the electron-phonon coupling elements of the conduction and valence bands. The difference of the two is fitted to the experimental data as 8 % of the individual valence band electron-phonon coupling elements. This is on the same order of magnitude as the estimations in³¹ which are based on DOS averaged *ab initio* calculations.

The second term occurs via the temperature difference as source and is found in agreement with previous thermal models (cf.^{28,32}). The thermal source acts via the lattice temperature change and causes an additional thermal expansion of the lattice which also impulsively excites oscillations of the nanoparticle and a shift in the equilibrium position particle radius. Within our model, the temperature changes were modeled using a two temperature model.^{28,32}

In order to solve the set of coupled partial differential equations they will be mapped on so-called Lamb modes $\mathbf{u}_{\text{nlm}}(\mathbf{r}) = \nabla \phi_{\text{nlm}}(\mathbf{r})$ with $\phi_{\text{nlm}}(\mathbf{r}) = j_l(\alpha_n r) P_l^m(\cos \theta) \exp\{im\varphi\}$ that character-

ize the vibrational modes of the a sphere.³³ As under the stress-free boundary assumptions those modes are not orthogonal, we expand the dynamics in the vibrational ground mode of the nanoparticle only. Hence, the expansion reads $\mathbf{u}(\mathbf{r}, t) = a(t) \mathbf{u}_0(\mathbf{r})$, $\rho_2^c(\mathbf{r}, t) = \rho(t) \phi_0(\mathbf{r})$ and the overlap normalization factor is $A = \int_{V_s} \phi_0^*(\mathbf{r}) \phi_0(\mathbf{r}) d^3r$ with the volume of the nanoparticle V_s . Using the projection, the equations simplify to ordinary differential equations which can numerically be integrated:

$$\partial_t \rho_2^c(t) = \frac{2e\epsilon_0}{\hbar A} \text{Im}\{\chi^{\text{inter}}(\omega_{\text{opt}})\} \int_{V_s} d^3r \mathbf{u}_0^*(\mathbf{r}) \cdot \nabla \left| \tilde{\mathbf{E}}_B(\mathbf{r}, t) \right|^2 - \frac{1}{\tau} \rho_2^c(t), \quad (17)$$

$$[\partial_t^2 + 2\gamma_{\text{ph}}\partial_t + \omega_0^2] a(t) = \zeta \rho_2^c(t) + \xi [T(t) - T_0]. \quad (18)$$

ϵ_d is the intraband Drude response of the background that is not incorporated in the interband susceptibility χ^{inter} . In order to compare with the experimental observations the relative oscillation $\mathbf{u}(\mathbf{R}, t)/|\mathbf{R}|$ where \mathbf{R} is chosen to be on the boundary of the sphere. Our numerical implementation allows to artificially switch the driving sources on and off which will allow to study their respective influence separately for various parameter regimes.

In Figure S5 we illustrate the the temporal behavior of $\rho_2^c(t)$ and the expected breathing mode amplitude after the optical excitation. The lifetime τ in Eq. (17) was fitted to the two-temperature model:

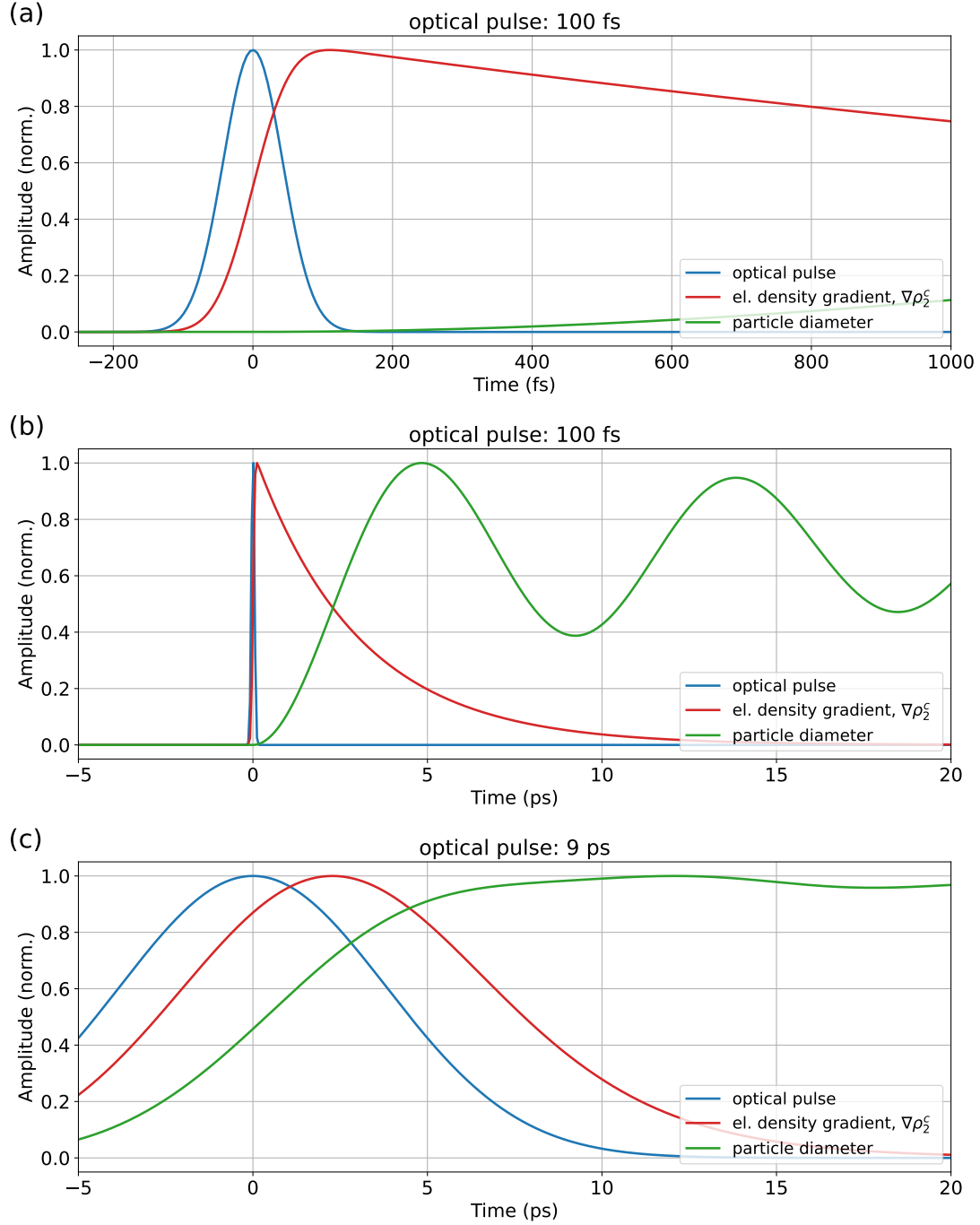


Figure S5: Temporal behavior of the electron density gradient coefficient in Eq. (17) after excitation with the optical pulse for two different optical pulse lengths: 100 fs in **a)**-**b)** (time windows: 1.2 ps and 25 ps, respectively) and 9 ps in **c)**.

3. Two-temperature model

The energy conversion within AuNPs by electron-phonon coupling is typically modeled in terms of the electron and lattice temperatures (T_e/T_l). Two coupled differential equations describe the change of the two temperatures with time:

$$C_e(T_e) \frac{\partial T_e}{\partial t} = -g(T_e - T_l) + \frac{W_0}{\sqrt{\pi}\sigma} \exp\{-t^2/\sigma^2\}, \quad (19)$$

$$C_l \frac{\partial T_l}{\partial t} = g(T_e - T_l) - (T_l - 298)/\tau_s, \quad (20)$$

where C_e and C_l are the electron and lattice heat capacities, respectively, g is the electron-phonon coupling constant. The last term in Eq. (19) is the source of hot electron excitation with the amplitude W_0 and width σ of the optical pulse. τ_s in Eq. (20) is the time constant for heat transfer from the phonon subsystem to the surrounding medium.^{34,35}

To simulate the electron and lattice temperature numerically using the two-temperature model, the lattice temperature was set to room temperature, while the initial electron temperature had to be calculated as follows: The initial jump in electronic temperature $\Delta T_{el}^{\text{initial}}$ depends on the absorbed energy per pump pulse and unit volume of Au:

$$\frac{I_{\text{abs}}}{N_{\text{AuNP}} \cdot V_{\text{AuNP}}} = \frac{1}{2} \gamma ((\Delta T_{el}^{\text{initial}} + T_{\text{RT}})^2 + (T_{\text{RT}})^2), \quad (21)$$

where I_{abs} is the absorbed energy per pump pulse according to Lambert-Beer's Law, N_{AuNP} is the number of AuNPs in the pump beam, V_{AuNP} is the volume of a AuNP of a given size, γ is the electron heat capacity for bulk gold and T_{RT} is the room temperature.³⁶

In this work, the absorbed energy per unit volume of Au was calculated based on the concentration of the particle solution and the absorbance determined by UV-Vis spectroscopy and the excitation power measured during the TA experiments. The e-ph coupling constant was taken from our previous work³⁷ and the electron and lattice heat capacities were taken from literature.^{31,38}

References

- (1) Zhang, Y.; He, S.; Guo, W.; Hu, Y.; Huang, J.; Mulcahy, J. R.; Wei, W. D. Surface-Plasmon-Driven Hot Electron Photochemistry. Chem. Rev. **2018**, 118, 2927–2954.
- (2) Schulz, F.; Pavelka, O.; Lehmkuhler, F.; Westermeier, F.; Okamura, Y.; Mueller, N. S.; Reich, S.; Lange, H. Structural order in plasmonic superlattices. Nature Communications **2020**, 11, 3821.
- (3) Haiss, W.; Thanh, N. T. K.; Aveyard, J.; Fernig, D. G. Determination of Size and Concentration of Gold Nanoparticles from UV-Vis Spectra. Anal. Chem. **2007**, 79, 4215–4221.
- (4) Hodak, J. H.; Martini, I.; Hartland, G. V. Spectroscopy and Dynamics of Nanometer-Sized Noble Metal Particles. J. Phys. Chem. B **1998**, 102, 6958–6967.
- (5) Erk, B. et al. CAMP@FLASH: an end-station for imaging, electron- and ion-spectroscopy, and pump–probe experiments at the FLASH free-electron laser. J. Synchrotron Radiat. **2018**, 25, 1529–1540.
- (6) Worbs, L.; Roth, N.; Lübke, J.; Estillore, A. D.; Xavier, P. L.; Samanta, A. K.; Küpper, J. Optimizing the geometry of aerodynamic lens injectors for single-particle coherent diffractive imaging of gold nanoparticles. J. Appl. Cryst. **2021**, 54, 1730–1737.
- (7) Roth, N.; Awel, S.; Horke, D. A.; Küpper, J. Optimizing aerodynamic lenses for single-particle imaging. J. Aerosol Sci. **2018**, 124, 17–29.
- (8) Redlin, H.; Al-Shemmary, A.; Azima, A.; Stojanovic, N.; Tavella, F.; Will, I.; Düsterer, S. The FLASH pump–probe laser system: Setup, characterization and optical beamlines. Nucl. Instrum. Methods Phys. Res. A **2011**, 635, S88–S93.
- (9) Strüder, L. et al. Large-format, high-speed, X-ray pnCCDs combined with electron and ion imaging spectrometers in a multipurpose chamber for experiments at 4th generation light sources. Nucl. Instrum. Methods Phys. Res. A **2010**, 614, 483–496.

- (10) Wiedorn, M. O. et al. Post-sample aperture for low background diffraction experiments at X-ray free-electron lasers. J Synchrotron Rad **2017**, 24, 1296–1298.
- (11) Awel, S.; Kirian, R. A.; Eckerskorn, N.; Wiedorn, M.; Horke, D. A.; Rode, A. V.; Küpper, J.; Chapman, H. N. Visualizing aerosol-particle injection for diffractive-imaging experiments. Opt. Express **2016**, 24, 6507–6521.
- (12) Krupin, O. et al. Temporal cross-correlation of x-ray free electron and optical lasers using soft x-ray pulse induced transient reflectivity. Opt. Express **2012**, 20, 11396–11406.
- (13) Roth, N. et al. New aerodynamic lens injector for single particle diffractive imaging. 2020; <http://arxiv.org/abs/2012.11237>.
- (14) Ayer, K.; Lan, T.-Y.; Elser, V.; Loh, N. D. Dragonfly: an implementation of the expand–maximize–compress algorithm for single-particle imaging. J. Appl. Cryst. **2016**, 49, 1320–1335.
- (15) Loh, N.-T. D.; Elser, V. Reconstruction algorithm for single-particle diffraction imaging experiments. Phys. Rev. E **2009**, 80, 026705.
- (16) Ayer, K. et al. 3D diffractive imaging of nanoparticle ensembles using an x-ray laser. Optica **2021**, 8, 15–23.
- (17) Johnson, P. B.; Christy, R.-W. Optical constants of the noble metals. Phys. Rev. B **1972**, 6, 4370.
- (18) Olmon, R. L.; Slovick, B.; Johnson, T. W.; Shelton, D.; Oh, S.-H.; Boreman, G. D.; Raschke, M. B. Optical dielectric function of gold. Phys. Rev. B **2012**, 86, 235147.
- (19) Madelung, O. Introduction to solid-state theory; Springer Science & Business Media: Berlin, Heidelberg, 2012; Vol. 2.

- (20) Czycholl, G. Theoretische Festkörperphysik Band 2: Anwendungen: Nichtgleichgewicht, Verhalten in äußeren Feldern, kollektive Phänomene; Springer-Verlag: Berlin, Heidelberg, 2017.
- (21) Lynn, J.; Smith, H.; Nicklow, R. Lattice dynamics of gold. Phys. Rev. B **1973**, 8, 3493.
- (22) Hannes, W.-R.; Meier, T. Higher-order contributions and nonperturbative effects in the non-degenerate nonlinear optical absorption of semiconductors using a two-band model. Phys. Rev. B **2019**, 99, 125301.
- (23) Haug, H.; Koch, S. W. Quantum theory of the optical and electronic properties of semiconductors; World Scientific Publishing Company: Singapore, 2009.
- (24) Wang, H.; Tam, F.; Grady, N. K.; Halas, N. J. Cu nanoshells: effects of interband transitions on the nanoparticle plasmon resonance. J. Phys. Chem. B **2005**, 109, 18218–18222.
- (25) Gross, E. K.; Runge, E. Many-particle theory; B.G. Teubner: Stuttgart, 1986.
- (26) Kittel, C.; Fong, C.-y. Quantum theory of solids; Wiley: New York, 1963; Vol. 5.
- (27) Sundararaman, R.; Narang, P.; Jermyn, A. S.; Goddard III, W. A.; Atwater, H. A. Theoretical predictions for hot-carrier generation from surface plasmon decay. Nat Commun **2014**, 5, 1–8.
- (28) Hartland, G. V. Coherent vibrational motion in metal particles: Determination of the vibrational amplitude and excitation mechanism. J. Chem. Phys. **2002**, 116, 8048–8055.
- (29) Hess, O.; Kuhn, T. Spatio-temporal dynamics of semiconductor lasers: Theory, modelling and analysis. Prog. Quantum. Electron. **1996**, 20, 85–179.
- (30) Etchegoin, P. G.; Le Ru, E.; Meyer, M. An analytic model for the optical properties of gold. J. Chem. Phys. **2006**, 125, 164705.

- (31) Brown, A. M.; Sundararaman, R.; Narang, P.; Goddard, W. A.; Atwater, H. A. Ab initio phonon coupling and optical response of hot electrons in plasmonic metals. Phys. Rev. B **2016**, 94, 075120.
- (32) Del Fatti, N.; Voisin, C.; Chevy, F.; Vallée, F.; Flytzanis, C. Coherent acoustic mode oscillation and damping in silver nanoparticles. J. Chem. Phys. **1999**, 110, 11484–11487.
- (33) Lamb, H. On the vibrations of an elastic sphere. Proc. London Math. Soc. **1881**, 1, 189–212.
- (34) Hartland, G. V. Optical Studies of Dynamics in Noble Metal Nanostructures. Chem. Rev. **2011**, 111, 3858–3887.
- (35) Allen, P. B. Theory of thermal relaxation of electrons in metals. Phys. Rev. Lett. **1987**, 59, 1460.
- (36) Guzelturk, B. et al. Nonequilibrium Thermodynamics of Colloidal Gold Nanocrystals Monitored by Ultrafast Electron Diffraction and Optical Scattering Microscopy. ACS Nano **2020**, 14, 4792–4804.
- (37) Staechelin, Y. U.; Hoeing, D.; Schulz, F.; Lange, H. Size-Dependent Electron–Phonon Coupling in Monocrystalline Gold Nanoparticles. ACS Photonics **2021**, 8, 752–757.
- (38) Ekici, O.; Harrison, R. K.; Durr, N. J.; Eversole, D. S.; Lee, M.; Ben-Yakar, A. Thermal analysis of gold nanorods heated with femtosecond laser pulses. J. Phys. D: Appl. Phys. **2008**, 41, 185501.